ACS APPLIED MATERIALS & INTERFACES

www.acsami.org

Research Article

Composition-Dependent Voltage-Driven OFF-ON Switching of Ferromagnetism in Co−Ni Oxide Microdisks

Aitor Arredondo-López, Konrad Eiler, Alberto Quintana, Gemma Rius, Irena Spasojevic, Asier Salicio, Aliona Nicolenco, Maria Lekka, Eva García-Lecina, Guillaume Brunin, David Waroquiers, Gian-Marco Rignanese, Eva Pellicer,* Enric Menéndez,* and Jordi Sort*

Cite This: *ACS Appl. Mater. Interfaces* 2025, 17, 9500−9513

Read Online

ACCESS | Metrics & More | Article Recommendations | Supporting Information

ABSTRACT: Magneto-ionics, which refers to the modification of the magnetic properties of materials through electric-field-induced ion migration, is emerging as one of the most promising methods to develop nonvolatile energy-efficient memory and spintronic and magnetoelectric devices. Herein, the controlled generation of ferromagnetism from paramagnetic Co−Ni oxide patterned microdisks (prepared upon thermal oxidation of metallic microdisks with dissimilar Co−Ni ratios, i.e., $Ni_{25}Co_{75}$ and $Ni_{50}Co_{50}$) is demonstrated under the action of voltage. The effect is related to the partial reduction of the oxide phases to their metallic forms. Samples richer in Co show stronger magneto-ionic activity, which manifests in lower-onset threshold voltages, faster switching rates, and larger values of the attained saturation magnetization. By means of scanning electron microscopy, a cobalt segregation phenomenon has been experimentally observed upon thermal oxidation, which has been theoretically discussed from the diffusivities' viewpoint. X-ray diffraction characterization has revealed transitions between purely mixed Ni and Co oxides, in the OFF state, to a mixture of oxide and metallic phases, in the ON state, because of the oxygen ion motion outward/inward the Co−Ni oxide microdisks, depending on the voltage polarity. *Ab initio* calculations reveal that the energy barrier for oxygen vacancy migration is lower in CoO than in NiO, in agreement with the obtained magneto-ionic responses. The observation of magneto-ionic effects in patterned disks (and not only in archetypical continuous films) is a step further for the practical utilization of this phenomenon in real miniaturized devices.

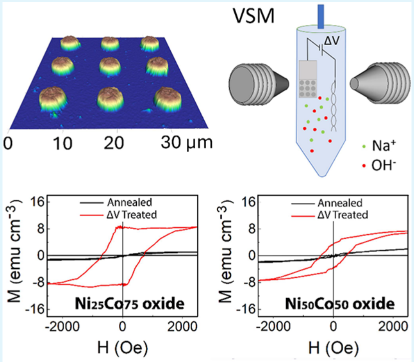

KEYWORDS: *Co−Ni oxide, magneto-ionics, ferromagnetism, cohesive energy, activation energy*

1. INTRODUCTION

The advent of Big Data has led to a growing demand for innovative data processing strategies aimed at enhancing energy efficiency in information and communication technologies (ICTs).[1−3] Traditionally, the switching of magnetic bits has relied on the use of electric currents. Initially, miniaturized electromagnets were developed to apply localized magnetic fields for this purpose. This was followed by devices that utilized spin-polarized electric currents to switch magnetization (*i.e.*, spin-transfer torque effect).[4] These actuation concepts have been successfully applied to boost performance of high-density hard disk drives and magneto-resistive random-access memories. However, since the underlying principle in both cases involves the use of electric currents, a significant fraction of the incoming power is dissipated in the form of heat due to the Joule effect. The limited energy efficiency is a significant obstacle for the further development of these technologies, particularly in nanoscale devices.[5] Alternatively, miniaturized systems relying on electric fields (*i.e.*, voltage) to manipulate magnetism instead of electric currents, by taking advantage of converse magnetoelectric effects, could provide a more energy-efficient methodology for storing magnetic data.[6] Such approach could be of particular interest in emerging areas such as neuromorphic computing.[7−10] Despite extensive research efforts, there is still a need of new materials to boost performance of low-power voltage-driven data storage/processing technologies.[11−14]

The ability to alter the magnetic properties of materials using electric fields has been demonstrated over the years. The development of single-phase multiferroics generated significant enthusiasm; however, these materials typically consist of complex oxides that exhibit their properties primarily at low temperatures.[15] Conversely, strain-mediated magnetoelectric coupling in ferroelectric/magnetostrictive composites (*i.e.*, multiferroic heterostructures) can be significant at room temperature. However, such mechanism is limited by fatigue effects, representing a bottleneck for the endurance of potential

Received: September 13, 2024
Revised: December 17, 2024
Accepted: December 27, 2024
Published: January 30, 2025

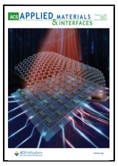

https://doi.org/10.1021/acsami.4c15739
ACS Appl. Mater. Interfaces 2025, 17, 9500−9513

strain-mediated spintronic devices.[16−18] Magnetoelectric effects caused by electrostatic surface charge accumulation (or carrier doping) are limited by the Thomas−Fermi electric field screening length in metals (on the order of 0.5 nm) or the Debye length in semiconductors (few nm), which means that such effects are only significant in ultrathin films.[19−25]

In recent years, a new phenomenon for the voltage control of magnetism, known as magneto-ionics (MI), has been investigated. This refers to changes of magnetic properties of materials arising from electric-field-driven ion (O^{2-}, F^-, N^{3-}, H^+, F^-, Li^+) migration. Under the action of the applied voltage (using either a solid or liquid electrolyte), ions diffuse from an ion reservoir to the adjacent MI target layer (or *vice versa*), modulating relevant magnetic properties, such as saturation magnetization (M_S), coercivity (H_C), Curie temperature, anisotropy easy axis, skyrmion density or other interfacial effects, such as exchange bias or the Ruderman−Kittel−Kasuya−Yosida (RKKY) interaction.[26−31] MI is advantageous since it induces nonvolatile changes of the aforementioned properties and its utilization is not limited to ultrathin films. Moreover, the induced effects can usually be reversed by applying voltage of opposite polarity. In liquid electrolyte-gated systems, MI effects are triggered by high electric fields generated across the so-called electric double layer (EDL). This ultrathin layer, typically of 0.5−1 nm thickness, is originated at the solid/liquid interface as a result of accumulation of charges of opposite sign upon voltage application.[32]

The vast majority of MI studies have focused on continuous films, with relatively less attention given to arrays of patterned structures, in spite of their technological interest for magnetic storage and microelectro-mechanical systems (MEMS). Microarrays of FeN,[33] CoPt disks/stripes,[34] FeO nanoislands,[35] Co/Gd_2O_3 nanopillars,[36] nanoporous FeO microdisks,[37] $CoFe_2O_4$ nanopillars,[38] nanopatterned CoO films grown on YSZ[39] or micropatterned FeCoN dots[40] are among the few examples of lithographed MI systems studied so far. Remarkably, in most of these cases, the thickness of the lithographed structures is limited to less than 100 nm. Studying MI effects in thicker dots is of interest for the implementation of voltage-controlled magnetic MEMS.

Concerning materials, those relying on voltage-driven O^{2-} diffusion remain the most extensively investigated. Contrary to the Fe-FeO_x system, in which a mixture of ferromagnetic and ferrimagnetic phases usually coexist, Co-CoO_x and Ni-NiO_x are interesting because their full oxidation, achieved by an applied voltage, can lead to full OFF (paramagnetic or antiferromagnetic) states. Transitions between ferromagnetic and non-ferromagnetic states (ON-OFF MI switching) have the potential to be used for synaptic applications (*i.e.*, potentiation/depression, multilevel memory),[7−10] stochastic computing or data security.[41] In addition, MI effects between ferromagnetic and antiferromagnetic phases are appealing for the voltage-control of exchange bias.

In this work, we investigate MI effects in patterned Co−Ni oxide disks. For this purpose, the behavior of patterned oxide disks with different Co/Ni ratios (i.e., Co−Ni−O) under voltage are studied, starting from an OFF state achieved by thermal oxidation of electrodeposited Co−Ni alloy disks in air. We show that upon voltage application, ferromagnetic behavior arises due to the partial reduction of the oxide phases and appearance of metallic Co and Ni. Moreover, we plunge into the critical influence of Ni on the voltage-driven ion motion. The switching rate at which ferromagnetism is generated, as well as the final attained magnetization (M), are found to decrease with the Ni content. *Ab initio* calculations of activation energies, used to provide deeper insights into the MI behavior, revealed distinct energy barriers for the oxygen vacancy migration as a function of Co−Ni stoichiometry.

2. EXPERIMENTAL SECTION/METHODS

2.1. Substrate Metallization. A cleaned 4-in. n-type Si wafer was sputtered with a buffer layer of Ti (10 nm)/Pt (80 nm) on an AJA International Inc. Sputtering system at room temperature under vacuum (3 mTorr). The Ti layer was deposited from a Ti target at 200 W (DC) for 10 s, after which a layer of Pt was sputtered at 100 W (DC) on top for 2 min.

2.2. UV Lithography and Electrodeposition of Co−Ni Microdisks. The metalized Si wafer underwent an optical lithography process to pattern arrays of 5-μm-diameter cylindrical cavities. Following substrate dehydration to volatilize possible organic components adhered to the surface, a 2-μm-thick HiPR6512 negative photoresist was spin-coated, followed by a soft bake. Next, the wafer was exposed to UV light in a Canon KSMA6 equipment and the photoresist development was performed with a HPRD28 developer. Finally, a hard bake was applied on a hot plate for 15 min at 115 °C. The wafer was sliced into pieces of 0.5 × 1 cm^2 for subsequent electrodeposition.

Electrodeposition was carried out in vessels of 1 L in a two-electrode cell configuration. Either unpatterned (for the growth of continuous films) or patterned (for the growth of microdisk arrays) Si/Ti/Pt substrates were used as the cathode and a Ni sheet as the anode. The electrolyte consisted of 500 g/L $Ni(SO_3NH_2)_2 \cdot 4H_2O$, 20 g/L $NiCl_2$, 25 g/L HBO_3, 5 mL/L NIMAC 12A Wetter surfactant (MacDermid-Enthone) and a $CoSO_4 \cdot 7H_2O$ concentration of 20 g/L. Co−Ni growth was carried out potentiostatically at 48 °C under stirring ($\boldsymbol{\omega}$ = 100 rpm). Microdisks with a mean composition of $Ni_{50}Co_{50}$ were obtained at a constant voltage of −3 V for 5 s, while those of a mean composition of $Ni_{25}Co_{75}$ were obtained at a voltage of −2.5 V for 5 s. Following electrodeposition, the samples were rinsed in Milli-Q water and dried under N_2 atmosphere.

2.3. Annealing in Air and Magnetoelectric Characterization. An annealing in air was done on samples of 0.5 × 1 cm^2 in size in a CARBOLITE tubular furnace at different temperatures and times, to ensure a completely nonmagnetic state. A LOT-QuantumDesign MicroSense Vibrating Sample Magnetometer (VSM) was used to characterize the magnetic properties of the samples after annealing. The magnetoelectric characterization of the samples was carried out in-plane at room temperature in the VSM under electrolyte gating, using an external power supply (Agilent B2902A). Voltages were applied between the Pt seed-layer of the samples (which served as the working electrode) and a platinum wire which acted as a counter electrode. The two electrodes were fit into an Eppendorf which was filled with propylene carbonate (Sigma-Aldrich 310328). PC was previously treated with metallic Na to remove traces of water, leaving Na^+ and OH^- ions behind.

2.4. Compositional & Structural Characterization. A Field-Emission Scanning Electron Microscope (FE-SEM, Zeiss Merlin) equipped with an energy dispersive X-ray (EDX) detector was used to characterize the oxide microdisk morphology and composition. Topographic SEM images were acquired at 5 keV, whereas EDX analyses were done at 15 keV. Cross sections were prepared by embedding the samples in a conductive epoxy resin followed by grinding to remove the resin until the cross-section was exposed to view, and polishing using an aqueous-based diamond suspension. The thickness of the disks was determined from the cross-sectional SEM images. $\theta/2\theta$ X-ray diffraction (XRD) patterns were recorded on a PANalytical X'pert Pro MRD (Materials Research Diffractometer) using Cu K_α radiation of λ = 0.154178 nm. The patterns were obtained in a 2θ range from 30° to 60°, with a step size of 0.026°. XRD patterns were Rietveld refined to obtain lattice cell parameters and crystallite sizes (average size of coherently diffracting domains).[42]

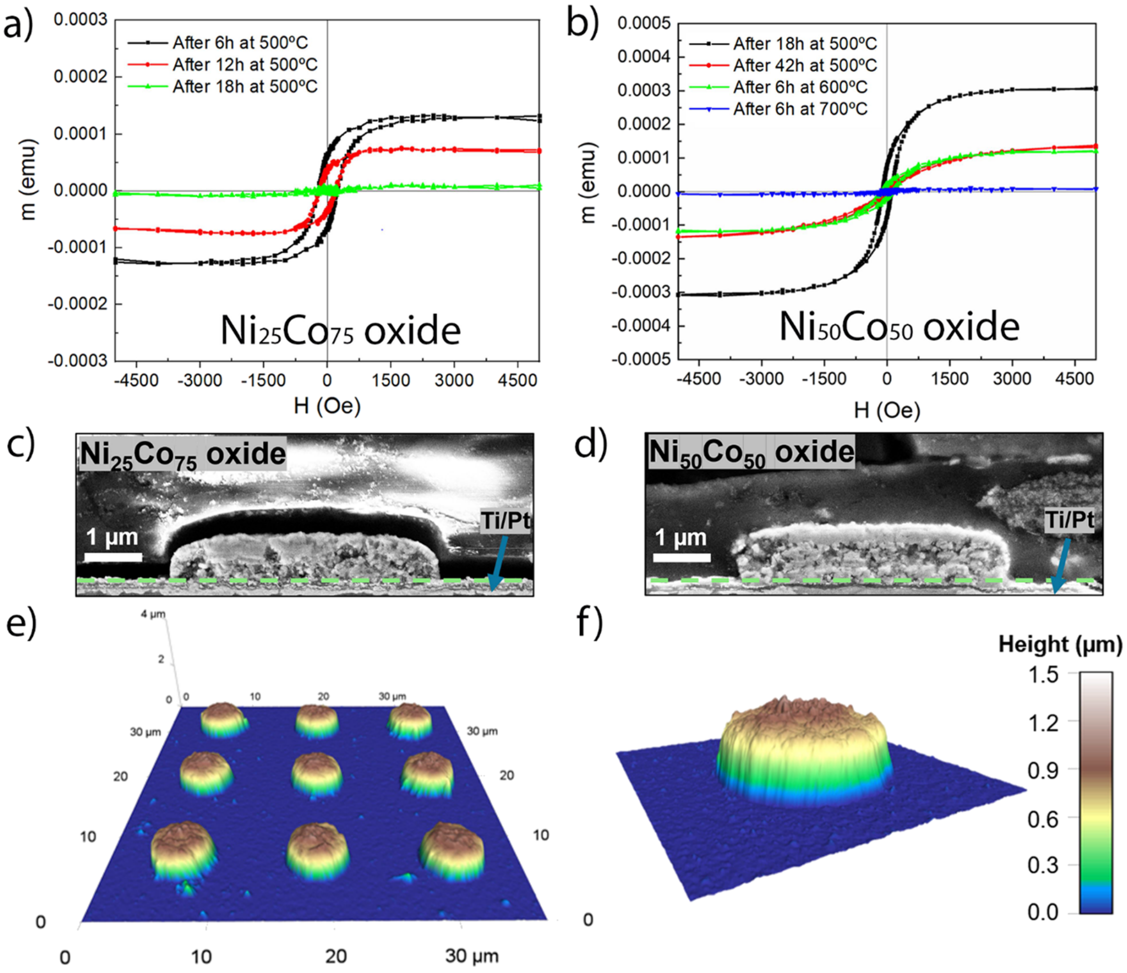

Figure 1. Room-temperature hysteresis loops acquired following annealing in air of the as-deposited (a) $Ni_{25}Co_{75}$ and (b) $Ni_{50}Co_{50}$ microdisk arrays at different temperature and times. SEM images of the cross-section of a single (c) $Ni_{25}Co_{75}$ and (d) $Ni_{50}Co_{50}$ microdisk following annealing of the samples at the corresponding optimal temperature and time. (e) 3D AFM topographical map of a 3 × 3 array of patterned $Ni_{25}Co_{75}$ oxide microdisks. (f) A topographical map of a single disk from the array.

X-ray photoelectron spectroscopy (XPS) experiments were performed on an ESFOSCAN equipment, which is based on a PHI 5000 VersaProbe instrument from Physical Electronics (ULVAC-PHI). Measurements were done with a monochromatic X-ray source (Aluminum K_α line of 1486.6 eV) calibrated using the $3d^{5/2}$ line of Ag with a full width at half-maximum of 0.6 eV. The analyzed area was a circle of 100 mm of diameter, and the selected resolution for the spectra was 224 eV of pass energy and 0.8 eV/step for the general spectra and 27 eV of pass energy and 0.1 eV/step for the high-resolution spectra of the selected elements. All measurements were made in in an ultrahigh vacuum (UHV) chamber at a pressure between 5×10^{-10} and 5×10^{-9} Torr. Prior to analysis, the utmost surface of the disks was sputtered with Ar ions for 4 min to remove contaminants. With the aim of collecting the Co 2p and Ni 2p core-level XPS spectra, the selected binding energy scan range was selected to be between 775 and 810 eV and between 850 and 887 eV, respectively. The spectra were corrected considering the position of carbon C 1s peak at 284.5 eV. Transmission electron microscopy (TEM) analyses were conducted on a cross-sectional lamella of a $Ni_{50}Co_{50}$ oxide microdisk, prepared by FIB, using a Thermo Fisher Scientific Spectra 300 (S)TEM double-corrected TEM operated at 200 kV.

2.5. Machine-Learned Molecular Dynamics. For each oxide (CoO, NiO, Co_3O_4, Ni_3O_4), the structures were first retrieved from the Materials Project database.[43,44] For molecular dynamics simulations, a > 1000 Å^3 volume supercell was generated and a single vacancy was created by removing a random O atom, giving a vacancy concentration around 10^{21} cm^{-3}. The supercell was relaxed using ASE[45] and the recently released CHGNet. Molecular dynamics simulations were carried out with ASE in the NVT ensemble (were the number of particles, volume and temperature are constant), with a time step of 2 fs and different temperatures, for a total simulation time of 2 ps. The mean square displacements are computed from the trajectory sampled every 50 timesteps using ASE, which is also used to plot the results.

2.6. First-Principles Calculations. Density Functional Theory (DFT) computations have been performed with Quantum ESPRESSO.[46] Norm-conserving pseudopotentials in the generalized-gradient approximation (GGA)[47] from the Pseudo-Dojo[48] have been used together with the PBE0 hybrid functional[49] adopting a 0.19 fraction of exact exchange to correctly account for the high correlation in the systems of interest and adequately represent the band gaps of antiferromagnetic NiO and CoO. The AFM ordering is along the [111] direction of the conventional unit cell. A structural relaxation is first performed starting from the structures retrieved from the Materials Project and using a Γ-centered 4 × 4 × 4 k-point mesh and a kinetic energy cutoff of 96 Ry. The supercell has been generated including 128 atoms, and an O atom has been removed. The distance between two O vacancies is larger than 10 Å to avoid spurious effects related to periodic images. Two neighboring vacancies are considered and atomic positions are relaxed in both cases (a single k-point, Γ, is then used). The nudged elastic band method with the climbing image approach[50,51] is then used to compute the minimum energy path between the two neighboring vacancy configurations and find the energy barrier between the two.

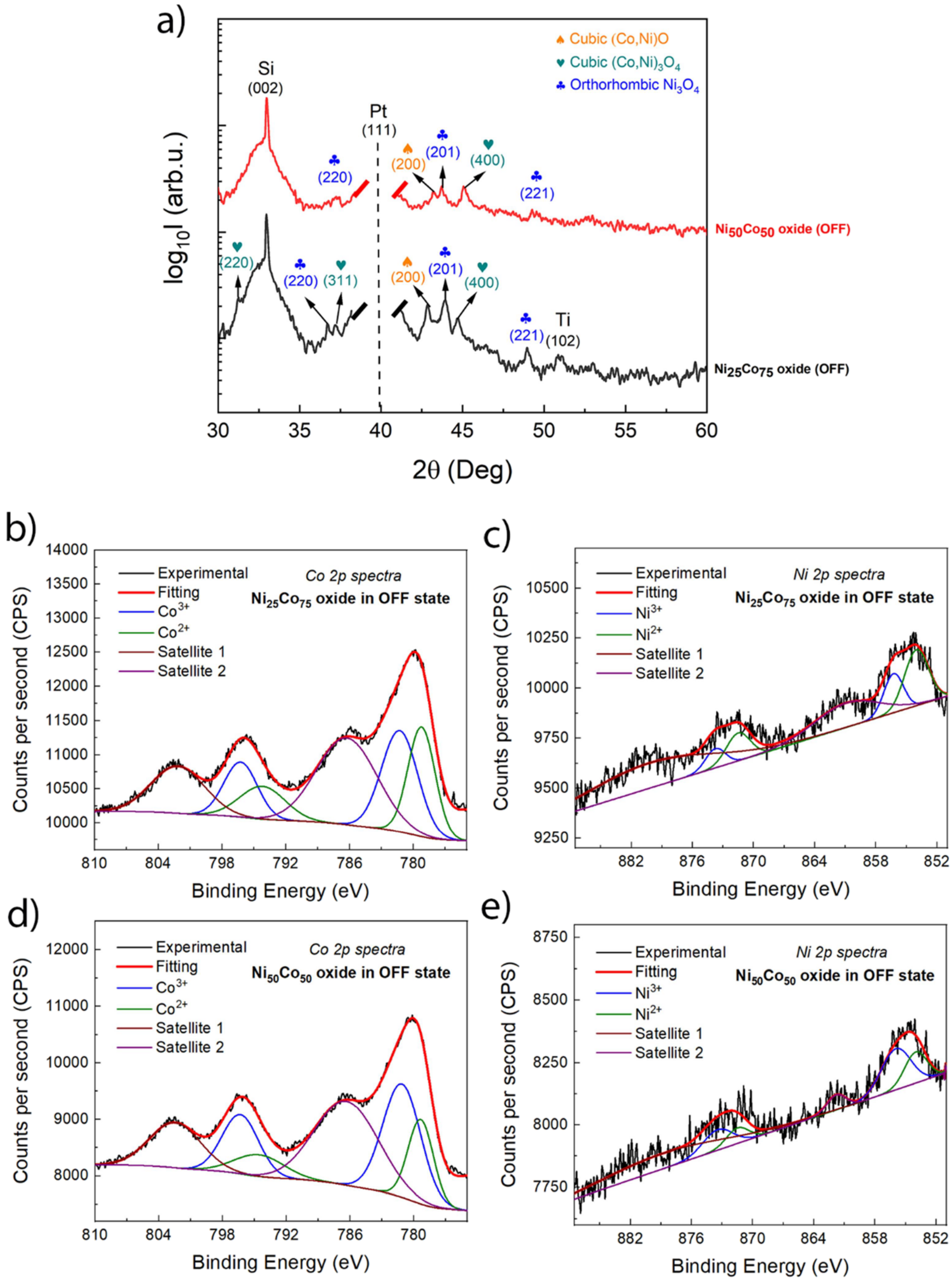

Figure 2. (a) XRD patterns of the $Ni_{25}Co_{75}$ and $Ni_{50}Co_{50}$ oxide microdisks in the OFF state (i.e., oxidized). (b, d) Co 2p and (c, e) Ni 2p core-level XPS spectra of the $Ni_{25}Co_{75}$ oxide and $Ni_{50}Co_{50}$ oxide microdisks, respectively.

3. RESULTS AND DISCUSSION

3.1. Synthesis of Paramagnetic Co–Ni Oxide Microdisk Arrays. Co–Ni alloy thick microdisks were synthesized by potentiostatic electrodeposition on photolithographed Si/Ti/Pt substrates. Two different voltages, namely −2.5 V and −3.0 V, were applied to obtain arrays of microdisks with varying Co/Ni ratio. The resulting microdisks had $Ni_{25}Co_{75}$ and $Ni_{50}Co_{50}$ stoichiometries, respectively, according to mean values obtained by EDX. The Co/Ni ratio in the disks was much higher than the [Co(II)]/[Ni(II)] in solution, in agreement with the anomalous-type codeposition of Co–Ni system from aqueous solutions.[52] Following resist removal, microdisks of 5 μm in diameter, matching the diameter of the lithographed cylindrical holes, and a thickness of 950 nm were obtained. To get an initial nonmagnetic (OFF) state prior to magneto-ionic studies, the samples were subjected to annealing in air. The target temperature and time to achieve an initial paramagnetic state was dependent on the Co/Ni ratio of the microdisks. An initial screening of annealing temperature and duration was needed to find the optimal working parameters: 18 h at 500 °C for the $Ni_{25}Co_{75}$ microdisk array, and 6 h at 700 °C for the $Ni_{50}Co_{50}$ counterparts. Figures 1a and 1b show the room-temperature hysteresis loops acquired following annealing of the as-deposited

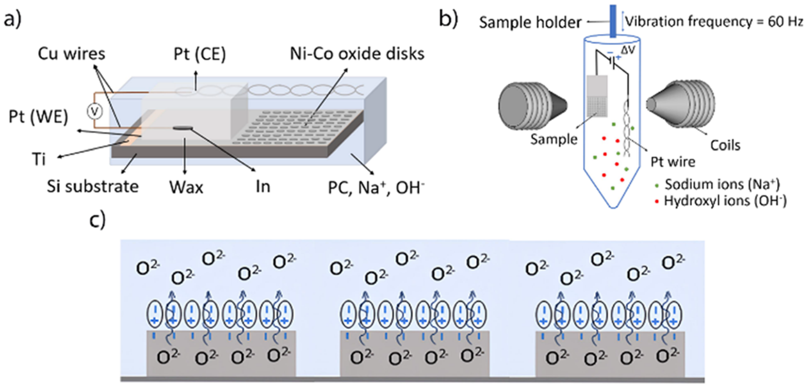

Figure 3. (a,b) Schematic representation of the electric contacts and the homemade cell setup for *in situ* liquid-gated VSM measurements, where WE and CE represent the working electrode and counter electrode, respectively. (c) Scheme showing the oxygen ion migration phenomenon on the microdisks viewed from the lateral side under application of negative voltage to the sample.

samples at varying temperatures and times. While the targeted OFF state was achieved upon annealing the $Ni_{25}Co_{75}$ microdisks at 500 °C for 18 h (green curve in Figure 1a), there is still a clear hysteresis loop for the $Ni_{50}Co_{50}$ microdisks when annealed under identical conditions (black curve in Figure 1b). Extending the annealing time to 42 h while keeping the same annealing temperature (500 °C) or increasing the annealing temperature to 600 °C led to a decrease in the magnetic moment at saturation, but a full OFF state was not achieved (red and green curves in Figure 1b). An OFF state was achieved at 700 °C and 6 h of annealing (blue curve in Figure 1b). Strictly speaking, the OFF state is not fully paramagnetic since a small coercive field is visible at low magnetic fields, suggesting that a small portion of the material remains incompletely oxidized.

Figures 1c and 1d show the cross-section SEM images of a single Co−Ni oxide microdisk after annealing, for the two studied compositions. The underlying Ti/Pt seed layer can be seen in the images. The corresponding EDX elemental mappings (Figure S1 of the Supporting Information) indicate that the distribution of cobalt and nickel is not uniform throughout the microdisk thickness. Namely, cobalt preferentially accumulates toward the uppermost surface of the microdisk, a phenomenon which is attributed to the annealing process since the distribution of Ni and Co elements in the as-deposited microdisks is uniform. Figure 1e displays a selected area of the Co−Ni oxide microdisks array after electrodeposition and annealing, while Figure 1f features the microscopic roughness level of one of the disks, both acquired by 3D AFM imaging.

The explanation of this cobalt migration phenomenon requires understanding both segregation and diffusion phenomena. For comparable 1-μm-thick oxide microdisks of both studied compositions, a combination of Mott-Cabrera's and Wagner's theories[53,54] applies effectively. These two theories assume the same scenario, i.e. a means by which the rate of oxide film growth relates to the diffusion coefficients. According to them, the electrochemical contact potential (*ECP*) difference between the adsorbed oxygen ions, which acquire negative charging, and the metal atoms, which accumulate a positive charging, creates an in-built electric field that induces ionic transport during the oxide growth. The schema resembles the one of a parallel plate capacitor. Essentially, these theories state that the lower the work function of a metallic ion, the more facile its migration will be through the oxide shell to combine with O_2. In our case, given that the work function of Co (5 eV) is lower than Ni (5.15 eV), the driving force for the segregation of Co atoms toward the topmost oxide shell of the disks will be larger than for Ni. The equations applied to calculate the ionic diffusion current (J) and the *ECP* are provided in the S.I. file, together with detailed parameters gathered in Table S1 and S2, respectively.

Calculation of the self-diffusion coefficients for Co and Ni in several phases of the Co−Ni oxide system is possible from values available in the literature. We found that self-diffusion coefficients are higher for Co than Ni regardless the phase and annealing temperature. This proves larger diffusivity of Co for both studied compositions, which tends to segregate toward the uppermost part of the oxide shell of the disks (see Tables S3 and S4 of the S.I. file).

Figure 2a shows the XRD patterns of the $Ni_{25}Co_{75}$ and $Ni_{50}Co_{50}$ oxide microdisk arrays at the OFF magnetic state (i.e., after annealing at 500 °C for 18 h and at 700 °C for 6 h, respectively). In both cases, complete oxidation of the as-deposited metallic microdisks is achieved. The remaining ferromagnetic fraction responsible for the small coercivity at low magnetic fields is likely below the detection limit of the technique (∼1 wt %). Besides the reflection ascribed to Si substrate (mp-149) and the seed-layer formed by Ti (mp-72) and Pt (mp-126), the rest of the peaks match orthorhombic Ni_3O_4 (mp-656887), Ni-substituted Co_3O_4 (mp-18748) and Ni-dissolved CoO (mp-19079). Hence, annealing of the samples at the chosen conditions yields a mixture of oxides. Note that the XRD peak labeling was carried out using the Materials Project database reference codes specified above.

Figures 2b-2e show the Co 2p and Ni 2p core-level XPS spectra of the microdisks. For the $Ni_{25}Co_{75}$ oxide microdisks, the Co 2p signal can be deconvoluted considering the presence of Co^{2+} and Co^{3+} (Figure 2b). These results are in agreement with the oxide phases encountered by XRD. The much higher intensity of the Co 2p signal with respect to Ni 2p is in agreement with the previously observed segregation of cobalt toward the microdisk surface upon annealing. The binding energy of 779.3 eV for Co $2p_{3/2}$ can be assigned to Co^{2+} oxidation state according to the literature.[55,56] Similarly, the Ni 2p signal could be deconvoluted considering Ni^{2+} and Ni^{3+} contributions (Figure 2c). The binding energy of 854.0 eV for Ni $2p_{3/2}$ matches Ni^{2+} oxidation state.[57,58]

Similar results were observed for the $Ni_{50}Co_{50}$ oxide microdisks, regarding the oxidation states of Co and Ni

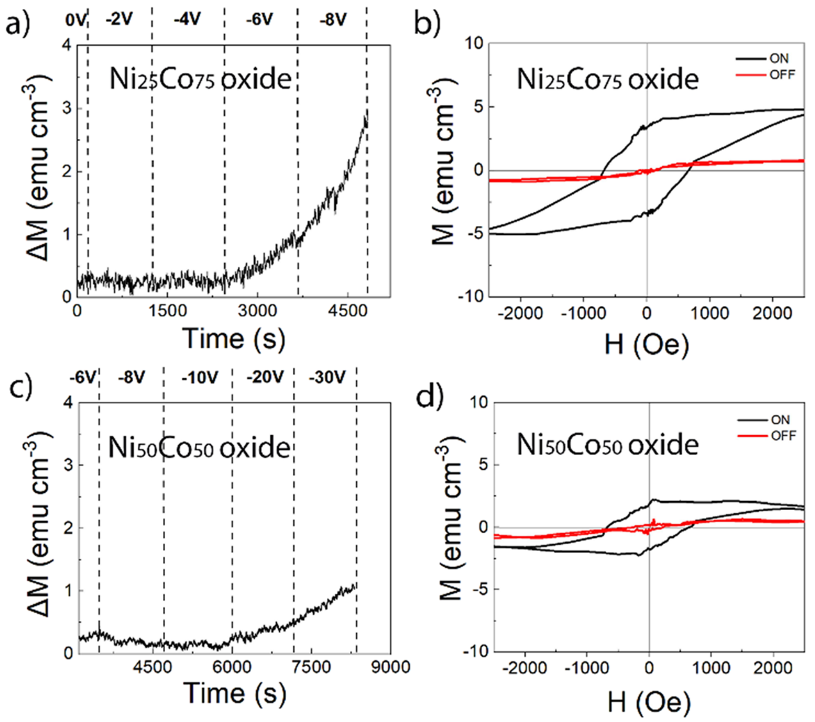

Figure 4. (a,c) Evolution of M as a function of time for the $Ni_{25}Co_{75}$ and $Ni_{50}Co_{50}$ oxide disks around the onset voltage. (b,d) Hysteresis loops acquired before voltage application (OFF) and after 20 min at the onset voltage (ON), for each of the compositions. Note that, for the sake of clarity, the starting time in (c) is 3000 s, although the same low voltage values/times were used as in the protocol applied in (a). No change of M was observed in (c) prior to 3000 s.

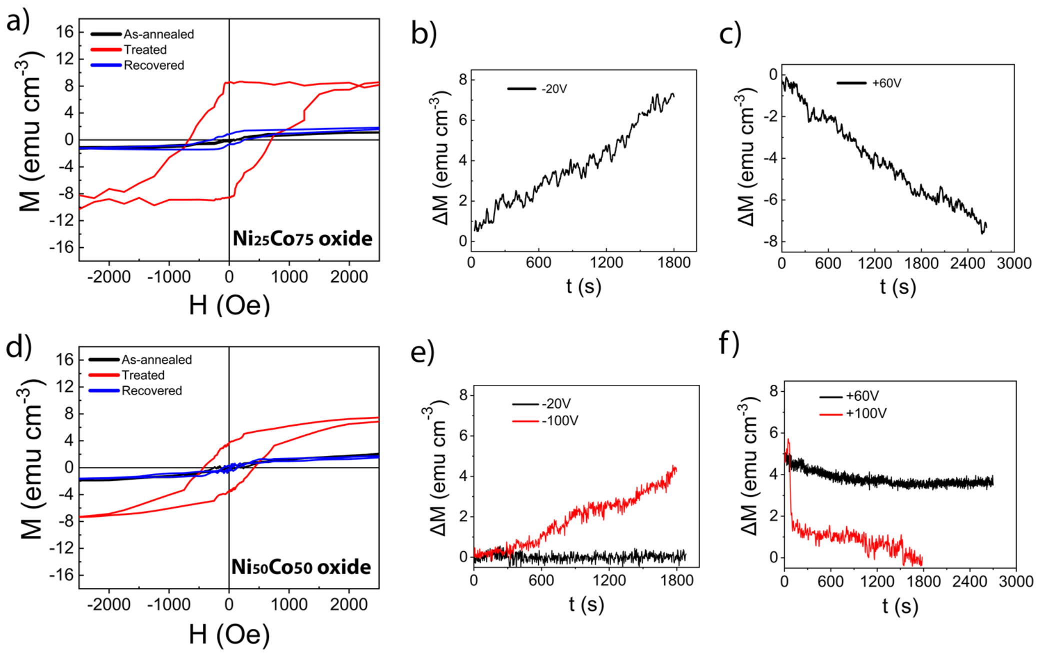

Figure 5. (a) VSM characterization of the $Ni_{25}Co_{75}$ oxide microdisks, demonstrating the comparison between the hysteresis loops in the as-annealed OFF (black), treated ON (red) and recovered re-OFF (blue) states. (b,c) Dependence of M on actuation time, during the respective negative and positive voltage steps. (d-f) display the same OFF-ON-OFF information for the $Ni_{50}Co_{50}$ oxide microdisks.

elements and the lower intensity of the Ni 2p signal compared to its Co 2p counterpart (Figures 2d and 2e).

3.2. Voltage-Induced Ferromagnetism in Patterned Co–Ni Oxide Disks. The magneto-ionic behavior of the two investigated microdisk arrays was assessed by VSM, applying voltage *in situ* using propylene carbonate (PC) as liquid electrolyte. Measurements of magnetic moment vs. time, as well as hysteresis loops, were recorded on the gated samples at room temperature. A scheme of the custom-made electrochemical cell setup used for these measurements is shown in Figure 3. The electrolytic cell was filled with PC, a polar nonaqueous liquid electrolyte, containing solvated Na^+ (5–25 ppm) and OH^- ions, resulting from immersion of a small portion of metallic Na and subsequent reaction with traces of water. The solvated ions contribute enhancing the strength of the EDL. Further details on the sample and the experimental setup are given in the Experimental section. All magnetic measurements were acquired as a function of applied voltage in an in-plane configuration (with magnetic field applied parallel to the surface of the film).

One of the typical features of magneto-ionic systems is the existence of an "onset voltage", *i.e.*, the threshold voltage beyond which magneto-ionic effects are triggered.[59] With the aim of determining the actual threshold voltage, the amplitude (i.e., absolute value) of the applied negative voltage was progressively increased, in steps of constant voltage, every 20 min. This allowed detecting the onset voltage, at which the system began to show ferromagnetic signal. During these measurements, the sample was subject to a constant external magnetic field of 1 T, to make sure that any generated ferromagnetic phase is fully saturated, so that all variations in the magnetic moment are directly related to the ferromagnetic phase percentage. The MI rates were determined from the initial slopes of the M vs. time curves.

As shown in Figure 4, very different threshold voltages were obtained for the two disk arrays with dissimilar compositions. While the Co-rich oxide disks exhibited the expected paramagnetic-ferromagnetic transition at reasonably low voltage values (−8 V), with a MI rate of $1.6 \cdot 10^{-3}$ emu cm^{-3} s^{-1}, the Ni-rich oxide disks required substantially larger voltage values (−30 V) to generate magnetization, at a lower MI rate of $5 \cdot 10^{-4}$ emu cm^{-3} s^{-1}. These empirical outcomes clearly indicated how MI weakens with the increase in the Ni content. To further confirm the role of Co content in increasing the MI rate, an array of microdisks with an intermediate composition ($Ni_{40}Co_{60}$) were prepared, annealed at 700 °C for 6 h and voltage-gated using the same procedure. An onset voltage of −14 V and a MI rate of $1.2 \cdot 10^{-3}$ emu cm^{-3} s^{-1} were obtained (Figure S3), falling in between the values of the other two compositions. The evolution of the onset voltage and the MI rate with the Co content in the disks is shown in panel (c) of the same figure.

The magnetic properties obtained at room temperature demonstrate not only the initial nonferromagnetic "OFF" state of the microdisk-patterned Co−Ni oxide samples, but also the possibility to switch them into ferromagnetic "ON" state. Figure 5 exhibits the full OFF-ON-OFF voltage-induced reversibility using representative voltage values. As it can be witnessed, larger voltages (both negative and positive) are required for the $Ni_{50}Co_{50}$ oxide disks, due to the less pronounced magneto-ionic effects in this case. Hence, it can be said that $Ni_{25}Co_{75}$ oxide disks show higher magneto-ionic activity, meaning that larger relative changes in sample's magnetization are attained over a specified period during electrochemical gating at a given constant external voltage. Importantly, for the same externally applied voltage, the electric field across the $Ni_{25}Co_{75}$ and $Ni_{50}Co_{50}$ oxide microdisks should, as a first approximation, be similar since the electric resistivity values of Co and Ni oxides at room temperature are near one another and their thicknesses are also comparable. Moreover, the top nm-thickness of the microdisks are Co-rich in both cases due to Co segregation upon annealing. Figure 5 reveals that reversible paramagnetic-to-ferromagnetic switchability was achieved in the two compositionally different samples. As for the $Ni_{25}Co_{75}$ oxide microdisks, liquid-electrolyte gating at −20 V for 30 min was used to switch from a nonferromagnetic to a ferromagnetic state (Figure 5b). An almost full recovery to the initial state was achieved upon applying a voltage of +60 V for 45 min (Figure 5c). Conversely, liquid-gating of the $Ni_{50}Co_{50}$ oxide microdisks at −20 V did not induce any change in the magnetization over the time of voltage application, i.e., substantially larger voltages were required. Eventually, the application of −100 V for 30 min provided the expected OFF-ON transition (Figure 5e). With the goal of making the recovery of this system comparable with the oxide microdisks with composition $Ni_{25}Co_{75}$, + 60 V were applied for 45 min. Nonetheless, this did not cause the expected full ON-OFF transition (Figure 5f), but only a slight decrease in the magnetization. Full recovery could only be achieved upon applying +100 V for 30 min. These results show that the electric-field-induced atomic-scale reconfiguration processes, although nonvolatile, can be magnetically reversed, and no other source of oxygen, besides the one incorporated in the disks upon annealing is required to induce the reported changes in magnetism. Nonvolatility was confirmed upon remeasuring the microdisk arrays for the two studied compositions 9 months after the OFF-ON magnetic transition took place. Remarkably, the ferromagnetic response remained virtually the same (see Figure S4 in the SI file), with just a slight decrease of the saturation magnetization by 10−14%.

In order to understand the origin of the induced ferromagnetism, structural characterization of the microdisks upon voltage treatment was done by XRD. Figure 6 shows the diffraction patterns for the $Ni_{25}Co_{75}$ oxide (Figure 6a) and the

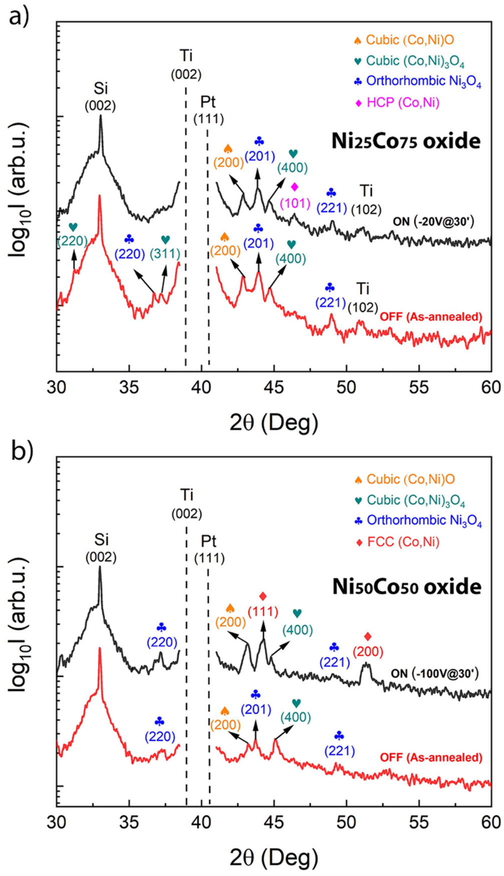

Figure 6. (a) XRD patterns of the $Ni_{25}Co_{75}$ oxide microdisks, at the steps prior (red pattern) and posterior (black pattern) to applying −20 V. (b) Same characterization for the $Ni_{50}Co_{50}$ oxide microdisks, upon applying −100 V for 30 min.

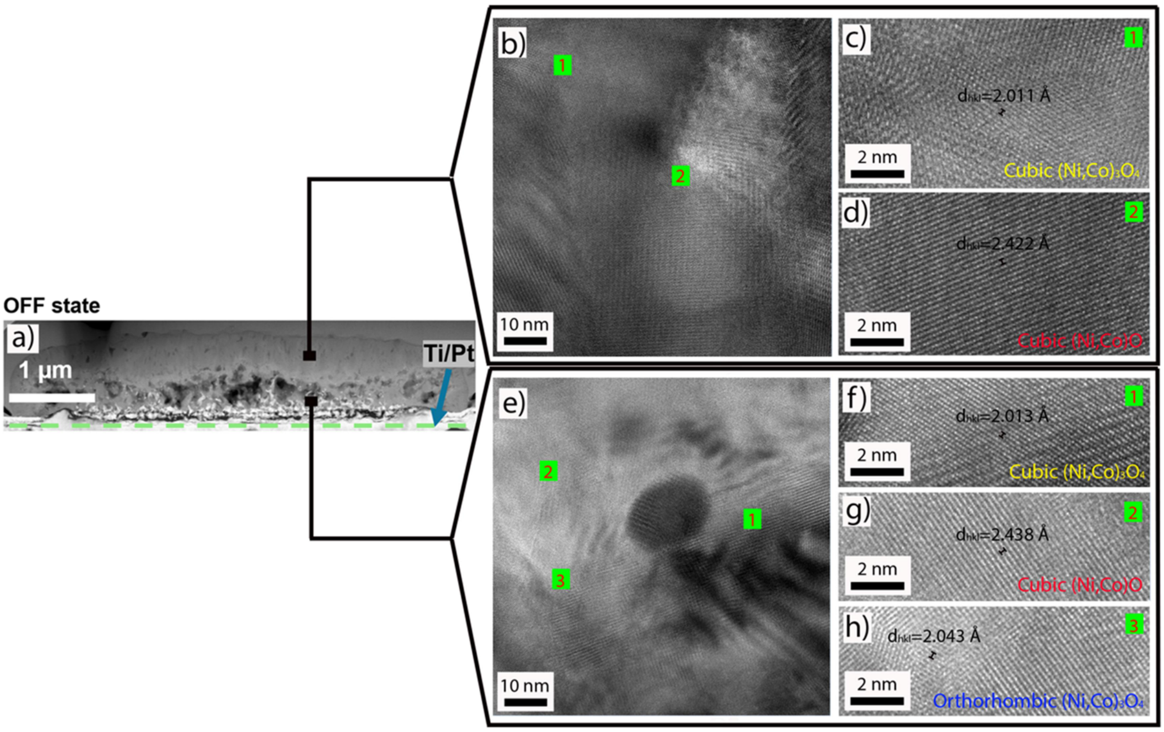

Figure 7. (a) Low magnification TEM image of a $Ni_{50}Co_{50}$ oxide microdisk in the OFF state, for which the location of the Ti/Pt seed-layer is indicated. (b) HRTEM image of the upper region of the disk along with (c, d) the analysis of the interplanar distances for the positions (1) and (2) indicated in (b). (e) HRTEM image of the bottom region of the disk along with (f-h) the analysis of the interplanar distances for the positions (1), (2) and (3) indicated in (e).

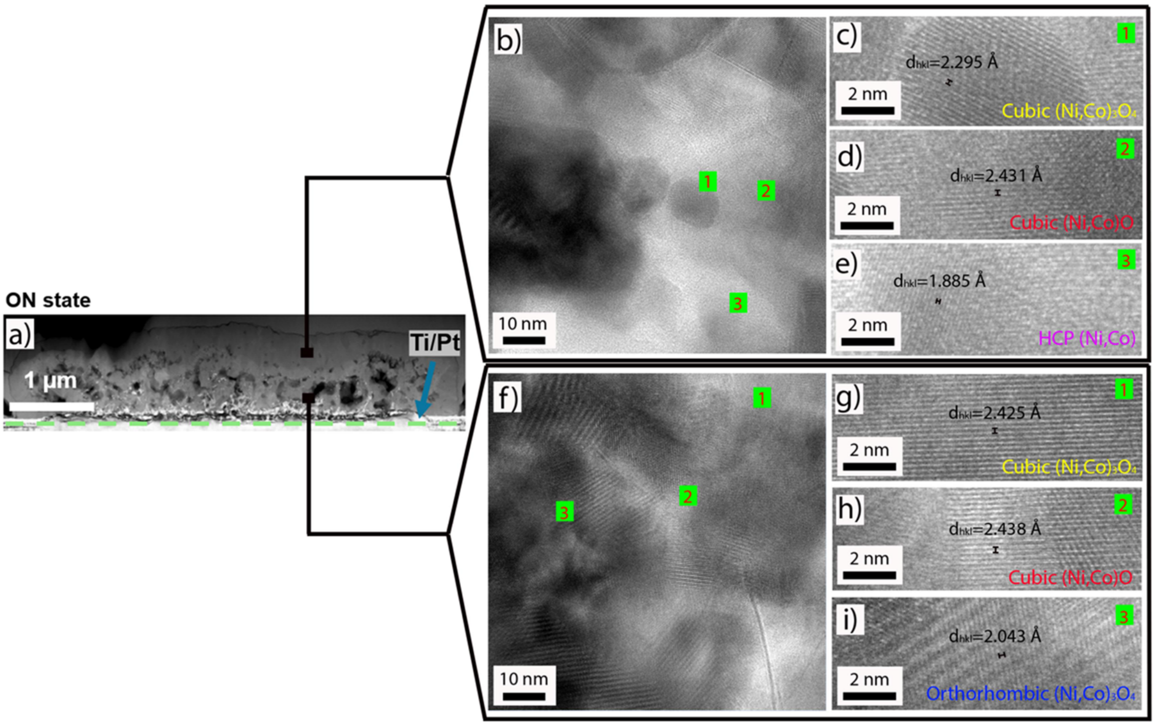

Figure 8. (a) Low magnification TEM image of a $Ni_{50}Co_{50}$ oxide microdisk in the ON state, for which the location of the Ti/Pt seed-layer is indicated. (b) HRTEM image of the upper region of the disk along with (c-e) the analysis of the interplanar distances for the positions (1), (2) and (3) indicated in (b). (f) HRTEM image of the bottom region of the disk along with (g-i) the analysis of the interplanar distances for the positions (1), (2) and (3) indicated in (f).

$Ni_{50}Co_{50}$ oxide (Figure 6b) microdisks, in both as-annealed and voltage-treated states. For the $Ni_{25}Co_{75}$ oxide microdisks, negative gating causes the suppression of the (220) and (311) peaks of the Ni-dissolved Co_3O_4. Conversely, the (101) peak corresponding to the dissolved Co−Ni HCP arises (mp-669382), which confirms the transition from purely mixed Ni

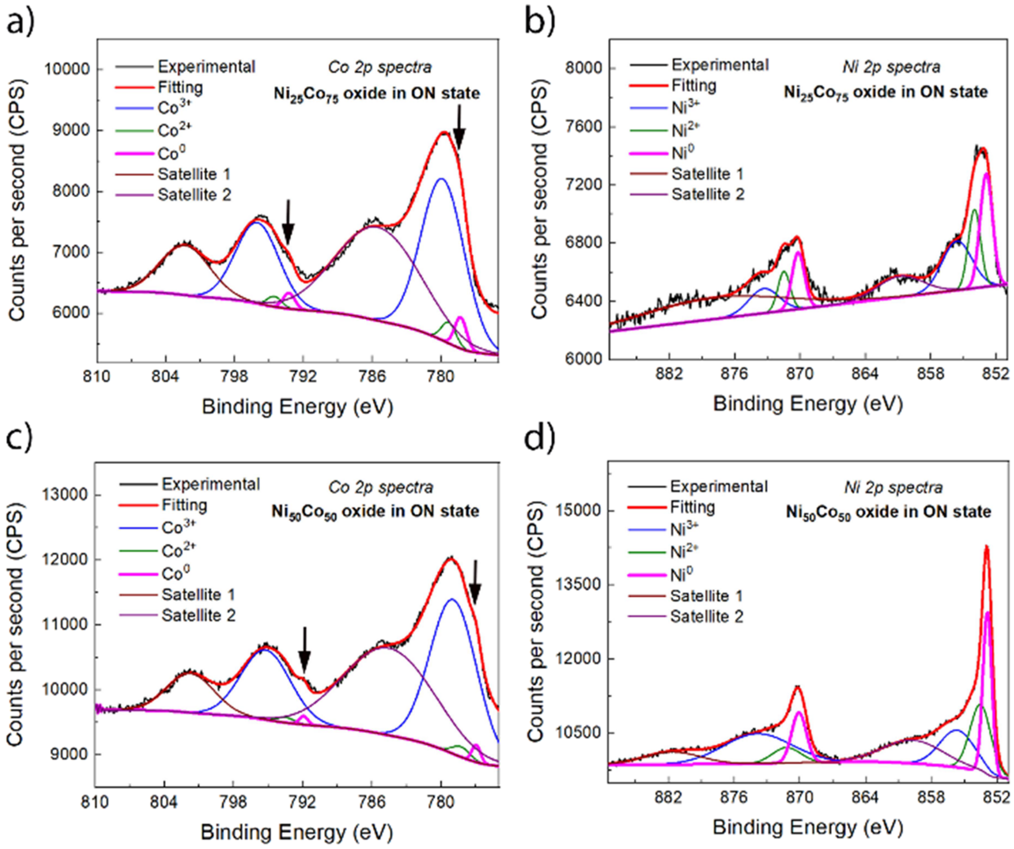

Figure 9. (a,c) Co 2p and (b,d) Ni 2p core-level XPS spectra of the $Ni_{25}Co_{75}$ oxide and $Ni_{50}Co_{50}$ oxide microdisks, after biasing the array at −20 V and −100 V, respectively.

and Co oxides to a combination of oxide and metallic phases in the ON state. These findings confirm the effective electrochemical reduction occurring after gating the sample in liquid at −20 V for 30 min, thus giving rise to the observed increase in magnetization. For the $Ni_{50}Co_{50}$ oxide microdisks, negative gating at −100 V for 30 min step results in the suppression of the (201) peak characteristic of orthorhombic Ni_3O_4. Conversely, the (111) and (200) peaks corresponding to dissolved FCC Co−Ni appear (mp-102), which again confirms the transition from purely mixed Ni and Co oxides to a combination of oxide and metallic phases in the ON state. A cross-section lamella of a $Ni_{50}Co_{50}$ oxide microdisk was prepared by FIB and characterized by HRTEM. Figure 7a shows the low magnification TEM of a single disk in the OFF state. HRTEM images (Figure 7b and 7c) were taken from the upper and bottom parts of the disk, in order to capture possible structural differences originating from the Co segregation previously observed by SEM. Interplanar distances matching cubic or orthorhombic Ni−Co oxides were found in all instances (Figure 7c,d,f-h). Meanwhile, similar HRTEM analyses of a $Ni_{50}Co_{50}$ oxide microdisk in the ON state (Figure 8) showed crystals located in the upper region of the disk whose interplanar distance matched HCP Co(Ni), as depicted in Figure 8e.

Complementary XPS analyses were carried out to confirm the findings from XRD and HRTEM (Figure 9). For both $Ni_{25}Co_{75}$ oxide and $Ni_{50}Co_{50}$ oxide microdisks, the Co 2p XPS core-level spectra show a contribution of Co^0 at an energy of 778.3 eV[60,61] (see black arrows in Figures 9a and 9c), in addition to Co^{2+} and Co^{3+} peaks. Similarly, the contribution of Ni^0 at an energy of 852.9 eV is evident according to the Ni 2p XPS spectra (Figures 9b and 9d), the position of which is in agreement with literature for metallic Ni.[62,63]

On the other hand, the satellite peaks at 786 and 803 eV in the Co 2p spectra,[64] and at 861 and 882 eV in the Ni 2p spectra,[65] originate from the degenerated magnetic spin states. Actually, these are linked to abrupt outer shell excitations given the perturbation of the central potential after photoionization of an inner electron.[66] Overall, the formation of metallic Co and Ni is thus responsible for the observed ferromagnetic response of the patterned microdisks upon negative voltage application.

Interestingly, a lower EDX signal intensity level for oxygen in the disks at ON state (cf. Figure S1 and Figure S2 of the S.I.) evidences that part of the oxygen was pulled out of the Co−Ni oxide disk upon negative biasing, hence leaving behind metallic Co and Ni clusters in the disk. This is consistent with the metallic cluster creation revealed by XRD, HRTEM and XPS analyses upon liquid-gated magnetoelectric treatments, both for $Ni_{25}Co_{75}$ oxide and $Ni_{50}Co_{50}$ oxide microdisks. The thicknesses of the microdisks were determined from cross-section SEM images, in which no change in thickness can be attributed upon applied voltage (cf. Figure S1 and S2).

3.3. Why the Incorporation of Ni Weakens MI Activity in the Co−Ni−O System. According to the experimental observations, the $Ni_{50}Co_{50}$ composition show the lowest MI activity. Considering the magnetic moments of Ni ($0.6\mu_B$) and Co ($1.72\mu_B$) atoms, the theoretical magnetic moments for $Ni_{25}Co_{75}$ and $Ni_{50}Co_{50}$ are $1.44\mu_B$ and $1.16\mu_B$, respectively. If no preferential reduction of Ni or Co in the microdisks is considered (i.e., the negative biasing yields metallic Co and Ni in the original stoichiometry) and if the amount of generated

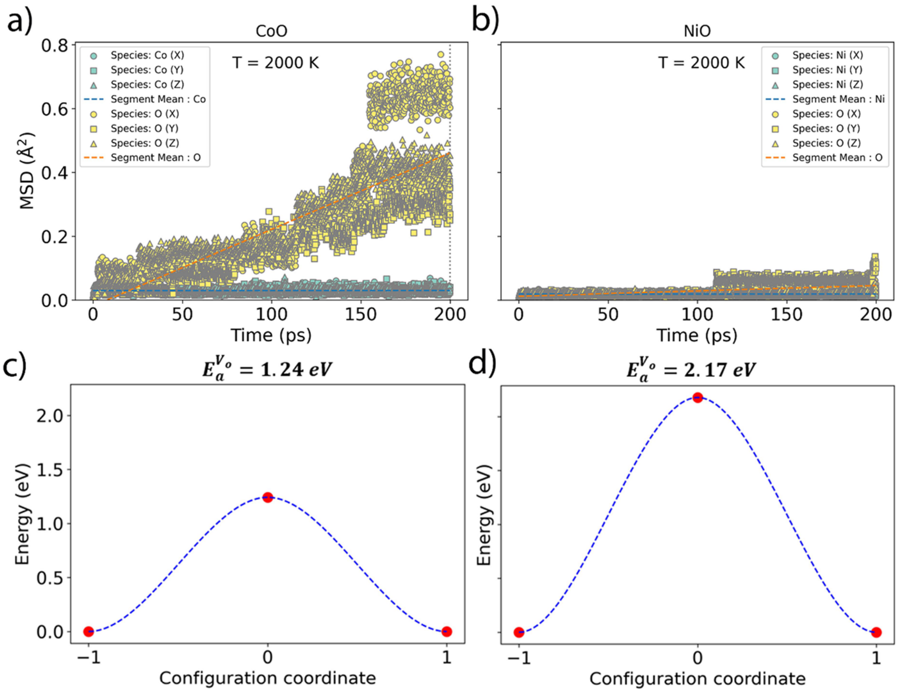

Figure 10. Computed mean square displacements of the different atoms at T = 2000 K, considering pure CoO (Figure 10a) and pure NiO (Figure 10b) with a single O vacancy. Figure 10c and 10d display the computed energy path of the O vacancy migration in CoO and NiO, respectively. The red dots have been computed while the line represents a cubic spline interpolation.

ferromagnetic alloy would be the same in both samples, this ratio should correspond to the experimentally measured M_S ratio between the two samples. However, the experimentally observed magnetic moments at saturation upon biasing the Co−Ni oxide films are M_S ($Ni_{25}Co_{75}$) = 60.5 emu cm^{-3} and M_S ($Ni_{50}Co_{50}$) = 37.5 emu cm^{-3} (Figure S7). The M_S ratio (1.61) is higher than the μ_B ratio (1.24), pointing to a larger amount of ferromagnetic alloy generated from the Co-rich mixed oxide (i.e., larger magneto-ionic effect), assuming that no preferential formation of metallic Co-rich clusters occurs in one of the samples (i.e., Co−Ni composition richer in Co than the stoichiometry before annealing).

Given that from a thermodynamic perspective Ni and Co are similar (their cohesive energy is practically the same), we aimed to tackle the kinetics behind their different oxygen migration capability. In order to explain the different MI behavior in $Ni_{25}Co_{75}$ and $Ni_{50}Co_{50}$ systems from a theoretical viewpoint, a combination of molecular dynamics using CHGNet,[67] a universal machine-learning interatomic potential (MLIP) and DFT calculations was carried out.

The O vacancy-induced mean square displacements of O atoms in cubic CoO and NiO were computed using molecular dynamics as reported in Figure 10. The large simulation temperatures used (2000 K) served to trigger more dynamic ion movement events during the given simulation time. The simulated temperatures for the aforementioned two systems, ranging from 1000 to 2000 K, are represented in Figure S5, while the cases of Ni_3O_4 and Co_3O_4 are represented in Figure S6 of the S.I. file. It is clear from Figure 10a and 10b that the O migration is easier in CoO than NiO, confirming what is experimentally observed. However, in addition to O atoms, Ni and Co atoms were also determined to migrate in the Co_3O_4 and Ni_3O_4 phases, which is in agreement with previous research works.[68] This can probably be attributed to the quality of the pretrained universal ML potential. Even though physical phenomena such as O migration can be described qualitatively using such universal MLIP, fine-tuning it to those specific systems would be necessary to reach quantitative results.

In order to quantify the difference between the migration of O ions in CoO and NiO, DFT was used to compute the energy barriers for O-vacancy migration in both systems. The results are reported in Figure 10c and 10d, namely the energy barrier is 1.24 eV in CoO and 2.17 eV in NiO. Considering that the phases and paths of migration in both systems are identical, we relate this difference to the different electronic structures of Co and Ni and their interaction with O atoms. Following Arrhenius' law, this leads to an O diffusion 2.5 times larger in CoO than in NiO, disregarding other differences.

This theoretical analysis confirms the larger MI activity in the Co-rich system, given its lower energy barrier for the oxygen vacancy to migrate through the lattice. As a means of better visualizing the phenomenon, $Ni_{25}Co_{75}$ and $Ni_{50}Co_{50}$ oxide continuous films with the same thickness of the disks were synthesized on unpatterned substrates, with the aim of comparing the MI under long-term constant voltage actuation. Details of the SEM characterization of cross-section of both films, along with their respective EDX elemental mappings and the comparison of MI activity in both compositional systems, are shown in Figure S7 of the SI. For a given biasing voltage of −100 V and upon long-term actuation, the continuous oxide film with larger Co content (i.e., $Ni_{25}Co_{75}$) results in a saturation magnetization of 60.5 emu cm^{-3}, while the film with lower Co content (i.e., $Ni_{50}Co_{50}$) leads to a value of 37.5 emu cm^{-3}. This larger magneto-ionic response with increasing Co content is in excellent agreement with the lower migration energy threshold for oxygen-vacancies in CoO than in NiO, obtained by molecular dynamics. Yet, for a given composition and applied voltage, in spite of their larger surface area, the performance of the microdisks is unexpectedly lower than their homologous continuous films (cf. Figure 5e and Figure S7). However, since the Pt layer between the disks is also exposed to the electrolyte, it probably partly screens the voltage at the surface of the Co−Ni oxide disks, thus explaining the lower magneto-ionic response. Despite the reduced performance, miniaturization of magneto-ionic systems is a step further toward the practical applications of this phenomenon in devices.

The curves in Figure S7 have been fitted using the Avrami formalism[69] to describe the evolution of the relative magnetization change (ΔM) with time (t):

$$\Delta M = \Delta M_S^{t\to\infty}\left(1 - e^{-k(t-t_0)^m}\right) \tag{1}$$

The following expressions for the two compositions studied have been obtained:

$$\Delta M_{Ni_{25}Co_{75}} = 60.5\cdot\left(1 - e^{-21.2\cdot 10^{-4}\cdot(t-115.1)^{0.91}}\right)$$

$$\Delta M_{Ni_{50}Co_{50}} = 37.5\cdot\left(1 - e^{-1.4\cdot 10^{-4}\cdot(t-74.0)^{1.34}}\right)$$

Upon comparing the m exponent values, the $Ni_{25}Co_{75}$ oxide film exhibits a lower value ($m = 0.91$) compared to its $Ni_{50}Co_{50}$ oxide counterpart ($m = 1.34$). This suggests that the electric-field-driven oxygen migration is more nucleation-dominated in the case of $Ni_{25}Co_{75}$ oxide since its m value is closer to 1. Given that the formation of metallic Co−Ni clusters under voltage arises from the nucleation of a few metallic Co−Ni unit cells, this difference in m values could explain why MI activity is stronger in the Co-rich samples.

4. CONCLUSIONS

A composition-dependent MI activity has been found in miniaturized Co−Ni oxide microdisks, obtained by electrodeposition onto a prelithographed substrate, followed by annealing in air. Upon negative in situ gating, the Co-rich system shows a larger MI rate, as compared to the Ni-rich system, as well as a lower threshold voltage for electric-field-induced oxygen motion. By combining molecular dynamics, a universal machine-learning interatomic potential and DFT calculations, a difference in the energy barriers for oxygen-vacancy migration has been obtained between pure CoO ($E_a^{O^{2-}}$= 1.24 eV) and pure NiO ($E_a^{O^{2-}}$= 2.17 eV). This theoretical outcome is consistent with the experimental in situ magnetometry results, both for the microscale patterned Co−Ni oxide disks as for their equivalent macroscale continuous films.

This work demonstrates the possibility of inducing OFF-ON-OFF switching of ferromagnetism at room temperature, by applying voltage, in relatively thick Co−Ni oxide microdisks, which can be of interest for novel magnetoelectric MEMS and other spintronic devices.

■ ASSOCIATED CONTENT

Supporting Information

The Supporting Information is available free of charge at https://pubs.acs.org/doi/10.1021/acsami.4c15739.

> Additional SEM-EDX characterization, magnetoelectric characterization of microdisk arrays with an intermediate Co−Ni oxide composition, calculated diffusion coefficient values, mean-square displacement plots, magnetoelectric characterization of continuous Co−Ni oxide films (PDF)

■ AUTHOR INFORMATION

Corresponding Authors

Eva Pellicer − *Departament de Física, Universitat Autònoma de Barcelona, Cerdanyola del Vallès 08193, Spain;* orcid.org/0000-0002-8901-0998; Email: eva.pellicer@uab.cat

Enric Menéndez − *Departament de Física, Universitat Autònoma de Barcelona, Cerdanyola del Vallès 08193, Spain;* Email: enric.menendez@uab.cat

Jordi Sort − *Departament de Física, Universitat Autònoma de Barcelona, Cerdanyola del Vallès 08193, Spain; Institució Catalana de Recerca i Estudis Avançats (ICREA), Barcelona 08010, Spain;* orcid.org/0000-0003-1213-3639; Email: jordi.sort@uab.cat

Authors

Aitor Arredondo-López − *Departament de Física, Universitat Autònoma de Barcelona, Cerdanyola del Vallès 08193, Spain*

Konrad Eiler − *Departament de Física, Universitat Autònoma de Barcelona, Cerdanyola del Vallès 08193, Spain;* orcid.org/0000-0001-8648-6395

Alberto Quintana − *Departament de Física, Universitat Autònoma de Barcelona, Cerdanyola del Vallès 08193, Spain;* orcid.org/0000-0002-9813-735X

Gemma Rius − *Instituto de Microelectrónica de Barcelona, Centro Nacional de Microelectrónica (IMB-CNM, CSIC), Cerdanyola del Vallès 08193, Spain*

Irena Spasojevic − *Departament de Física, Universitat Autònoma de Barcelona, Cerdanyola del Vallès 08193, Spain*

Asier Salicio − *Basque Research and Technology Alliance (BRTA), CIDETEC, Donostia-San Sebastián 20014, Spain*

Aliona Nicolenco − *Basque Research and Technology Alliance (BRTA), CIDETEC, Donostia-San Sebastián 20014, Spain*

Maria Lekka − *Basque Research and Technology Alliance (BRTA), CIDETEC, Donostia-San Sebastián 20014, Spain*

Eva García-Lecina − *Basque Research and Technology Alliance (BRTA), CIDETEC, Donostia-San Sebastián 20014, Spain*

Guillaume Brunin − *A6K Engineering Center, MATGENIX, Charleroi 6000, Belgium*

David Waroquiers − *A6K Engineering Center, MATGENIX, Charleroi 6000, Belgium*

Gian-Marco Rignanese − *A6K Engineering Center, MATGENIX, Charleroi 6000, Belgium; Institute of Condensed Matter and Nanosciences (IMCN), Louvain-la-Neuve 1348, Belgium*

Complete contact information is available at: https://pubs.acs.org/10.1021/acsami.4c15739

Author Contributions

The manuscript was written through contributions of all authors. All authors have given approval to the final version of the manuscript.

Funding

This work has received funding from Horizon Europe under grant agreement No. 101058076-NICKEFFECT.

Notes

The authors declare no competing financial interest.

■ ACKNOWLEDGMENTS

The authors also acknowledge financial support from PID2020-116844RB-C21, PID2020 116844RB-C22, 2021-SGR-00651, MCIN/AEI/10.13039/501100011033 and European Union NextGeneration/PRTR (grant CNS2022-135230), PDC2021-

121276-C31, PDC2021-121276-C32 and the European Research Council (2021-ERC-Advanced "REMINDS" *N*° 101054687) grants. E.M. is a Serra Húnter Fellow. G.R. acknowledges Ayudas Ramon y Cajal ref. RyC-2026-21412 and access to the Spanish ICTS Network MICRONANOFABS. The IMB-CNM-CSIC is supported by the María de Maetzu Centres of Excellence programme ref. CEX2023-001397-M funded by MCINN-AEI. We also acknowledge the equipment and service provided by the Surface Analysis Unit of the CCiTUB in the work for the XPS analysis carried out. The HRTEM characterization was performed at ALBA Synchrotron with the collaboration of ALBA staff.

■ REFERENCES

(1) Žutić, I.; Fabian, J.; Das Sarma, S. Spintronics: Fundamentals and applications. *Rev. Mod. Phys.* **2004**, *76* (2), 323−410.

(2) Wolf, S. A.; Awschalom, D. D.; Buhrman, R. A.; Daughton, J. M.; von Molnár, S.; Roukes, M. L.; Chtchelkanova, A. Y.; Treger, D. M. Spintronics: a spin-based electronics vision for the future. *Sci.* **2001**, *294* (5546), 1488−1495.

(3) Chappert, C.; Fert, A.; Van Dau, F. N. The emergence of spin electronics in data storage. *Nat. Mater.* **2007**, *6* (11), 813−823.

(4) Dieny, B.; Sousa, R. C.; Herault, J.; Papusoi, C.; Prenat, G.; Ebels, U.; Houssameddine, D.; Rodmacq, B.; Auffret, S.; Prejbeanu, L. D. B.; Cyrille, M. C.; Delaet, B.; Redon, O.; Ducruet, C.; Nozieres, J. P.; Prejbeanu, I. L. Spin-transfer effect and its use in spintronic components. *Int. J. Nanotechnol.* **2010**, *7*, 591.

(5) Shiota, Y.; Nozaki, T.; Bonell, F.; Murakami, S.; Shinjo, T.; Suzuki, Y. Induction of coherent magnetization switching in a few atomic layers of FeCo using voltage pulses. *Nat. Mater.* **2012**, *11* (1), 39−43.

(6) Hu, J.-M.; Nan, C.-W. Opportunities and challenges for magnetoelectric devices. *APL Mater.* **2019**, *7* (8), No. 080905.

(7) Mishra, R.; Kumar, D.; Yang, H. Oxygen-Migration-Based Spintronic Device Emulating a Biological Synapse. *Phys. Rev. Applied* **2019**, *11*, No. 054065.

(8) Tan, Z.; de Rojas, J.; Martins, S.; Lopeandía, A.; Quintana, A.; Cialone, M.; Herrero Martín, J.; Meersschaut, J.; Vantomme, A.; Costa Krämer, J. L.; Sort, J.; Menéndez, E. Frequency-dependent stimulated and post-stimulated voltage control of magnetism in transition metal nitrides: towards brain-inspired magneto-ionics. *Mater. Horiz.* **2023**, *10*, 88−96.

(9) Monalisha, P.; Ma, Z.; Pellicer, E.; Menéndez, E.; Sort, J. A Multilevel Magnetic Synapse Based on Voltage-Tuneable Magnetism by Nitrogen Ion Migration. *Adv. Electron. Mater.* **2023**, *9* (8), No. 2300249.

(10) Guan, Y.; Han, H.; Li, F.; Li, G.; Parkin, S. Ionic Gating for Tuning Electronic and Magnetic Properties. *Annu. Rev. Mater. Res.* **2023**, *53*, 25−51.

(11) Xia, Q.; Yang, J. J. Memristive crossbar arrays for brain-inspired computing. *Nat. Mater.* **2019**, *18* (5), 518.

(12) Torrejon, J.; Riou, M.; Araujo, F. A.; Tsunegi, S.; Khalsa, G.; Querlioz, D.; Bortolotti, P.; Cros, V.; Yakushiji, K.; Fukushima, A.; Kubota, H.; Yuasa, S.; Stiles, M. D.; Grollier, J. Neuromorphic computing with nanoscale spintronic oscillators. *Nat.* **2017**, *547* (7664), 428−431.

(13) Song, C.; Cui, B.; Li, F.; Zhou, X.; Pan, F. Recent progress in voltage control of magnetism: Materials, mechanisms, and performance. *Prog. Mater. Sci.* **2017**, *87*, 33−82.

(14) Duschek, K.; Pohl, D.; Fahler, S.; Nielsch, K.; Leistner, K. Research Update: Magnetoionic control of magnetization and anisotropy in layered oxide/metal heterostructures. *APL Mater.* **2016**, *4*, No. 032301.

(15) Lu, C.; Hu, W.; Tian, Y.; Wu, T. Multiferroic oxide thin films and heterostructures. *Appl. Phys. Rev.* **2015**, *2*, No. 021304.

(16) Brivio, S.; Petti, D.; Bertacco, R.; Cezar, J. C. Electric field control of magnetic anisotropies and magnetic coercivity in Fe/$BaTiO_3$ (001) heterostructures. *Appl. Phys. Lett.* **2011**, *98*, No. 092505.

(17) Liu, Y.; Hu, F. X.; Zhang, M.; Wang, J.; Shen, F. R.; Zuo, W. L.; Zhang, J.; Sun, J. R.; Shen, B. G. Electric field control of magnetic properties of $Nd_2Fe_{14}B$ thin films grown onto PMNPT substrates. *Appl. Phys. Lett.* **2017**, *110*, No. 022401.

(18) Fina, I.; Quintana, A.; Padilla-Pantoja, J.; Martí, X.; Macia, J.; Sanchez, F.; Foerster, M.; Aballe, L.; Fontcuberta, J.; Sort, J. Electric-Field-Adjustable Time-Dependent Magnetoelectric Response in Martensitic FeRh Alloy. *ACS Appl. Mater. Interfaces* **2017**, *9* (18), 15577−15582.

(19) Weisheit, M.; Fähler, S.; Marty, A.; Souche, Y.; Poinsignon, C.; Givord, D. Electric field-induced modification of magnetism in thin-film ferromagnets. *Science* **2007**, *315* (5815), 349−351.

(20) Koyama, T.; Chiba, D. Influence of the magnetization reversal mechanism on the electric field modulation of coercivity in Pt/Co structures. *Phys. Rev. B* **2017**, *96*, No. 224409.

(21) Chiba, D.; Ono, T. Control of magnetism in Co by an electric field. *J. Phys. D: Appl. Phys.* **2013**, *46*, No. 213001.

(22) Chiba, D.; Fukami, S.; Shimamura, K.; Ishiwata, N.; Kobayashi, K.; Ono, T. Electrical control of the ferromagnetic phase transition in cobalt at room temperature. *Nat. Mater.* **2011**, *10* (11), 853−856.

(23) Maruyama, T.; Shiota, Y.; Nozaki, T.; Ohta, K.; Toda, N.; Mizuguchi, M.; Tulapurkar, A. A.; Shinjo, T.; Shiraishi, M.; Mizukami, S.; Ando, Y.; Suzuki, Y. Large voltage-induced magnetic anisotropy change in a few atomic layers of iron. *Nat. Nanotechnol.* **2009**, *4* (3), 158−161.

(24) Zhang, H.; Richter, M.; Koepernik, K.; Opahle, I.; Tasnadi, F.; Eschrig, H. Electric-field control of surface magnetic anisotropy: a density functional approach. *New J. Phys.* **2009**, *11*, No. 043007.

(25) Yang, Q.; Wang, L.; Zhou, Z.; Wang, L.; Zhang, Y.; Zhao, S.; Dong, G.; Cheng, Y.; Min, T.; Hu, Z.; Chen, W.; Xia, K.; Liu, M. Ionic liquid gating control of RKKY interaction in FeCoB/Ru/FeCoB and $(Pt/Co)_2/Ru/(Co/Pt)_2$ multilayers. *Nat. Commun.* **2018**, *9*, 991.

(26) Navarro-Senent, C.; Quintana, A.; Menéndez, E.; Pellicer, E.; Sort, J. Electrolyte-gated magnetoelectric actuation: Phenomenology, materials, mechanisms, and prospective applications. *APL Mater.* **2019**, *7*, No. 030701.

(27) Molinari, A.; Hahn, H.; Kruk, R. Voltage-Control of Magnetism in All-Solid-State and Solid/Liquid Magnetoelectric Composites. *Adv. Mater.* **2019**, *31*, No. 1806662.

(28) Robbennolt, S.; Menéndez, E.; Quintana, A.; Gómez, A.; Auffret, S.; Baltz, V.; Pellicer, E.; Sort, J. Reversible, Electric-Field Induced Magneto-Ionic Control of Magnetism in Mesoporous Cobalt Ferrite Thin Films. *Sci. Rep* **2019**, *9*, 10804.

(29) de Rojas, J.; Quintana, A.; Lopeandía, A.; Salguero, J.; Muñiz, B.; Ibrahim, F.; Chshiev, M.; Nicolenco, A.; Liedke, M. O.; Butterling, M.; Wagner, A.; Sireus, V.; Abad, L.; Jensen, C. J.; Liu, K.; Nogués, J.; Costa-Krämer, J. L.; Menéndez, E.; Sort, J. Voltage-driven motion of nitrogen ions: a new paradigm for magneto-ionics. *Nat. Commun.* **2020**, *11*, 5871.

(30) Ma, Z.; Fuentes-Rodriguez, L.; Tan, Z.; Pellicer, E.; Abad, L.; Herrero-Martín, J.; Menéndez, E.; Casañ-Pastor, N.; Sort, J. Wireless magneto-ionics: voltage control of magnetism by bipolar electrochemistry. *Nat. Commun.* **2023**, *14*, 6486.

(31) Syskaki, M. A.; Dohi, T.; Bednarz, B.; Filnov, S. O.; Kasatikov, S. A.; Bhukta, M.; Smekhova, A.; Pachat, R.; van der Jagt, J. W.; Ono, S.; Ravelosona, D.; Langer, J.; Kläui, M.; Herrera Diez, L.; Jakob, G. Magneto-ionic modulation of the interlayer exchange interaction in synthetic antiferromagnets. *Appl. Phys. Lett.* **2024**, *124* (8), No. 082408.

(32) Zhan, H.; Cervenka, J.; Prawer, S.; Garrett, D. J. Electrical Double Layer at Various Electrode Potentials: A Modification by Vibration. *J. Phys. Chem. C* **2017**, *121* (8), 4760−4764.

(33) de Rojas, J.; Quintana, A.; Rius, G.; Stefani, C.; Domingo, N.; Costa-Krämer, J. L.; Menéndez, E.; Sort, J. Voltage control of magnetism with magneto-ionic approaches: Beyond voltage-driven oxygen ion migration. *Appl. Phys. Lett.* **2022**, *120* (7), No. 070501.

(34) Navarro-Senent, C.; Fornell, J.; Isarain-Chávez, E.; Quintana, A.; Menéndez, E.; Foerster, M.; Aballe, L.; Weschke, E.; Nogués, J.; Pellicer, E.; Sort, J. Large Magnetoelectric Effects in Electrodeposited

Nanoporous Microdisks Driven by Effective Surface Charging and Magneto-Ionics. *ACS Appl. Mater. Interfaces.* **2018**, *10*, 44897−44905.

(35) Duschek, K.; Petr, A.; Zehner, J.; Nielsch, K.; Leistner, K. All-electrochemical voltage-control of magnetization in metal oxide/metal nanoislands. *J. Mater. Chem. C* **2018**, *6*, 8411.

(36) Chen, Y.; Nicolenco, A.; Molet, P.; Mihi, A.; Pellicer, E.; Sort, J. Magneto-ionic suppression of magnetic vortices. *Sci. Technol. Adv. Mater.* **2021**, *22* (1), 972−984.

(37) Cialone, M.; Nicolenco, A.; Robbennolt, S.; Menéndez, E.; Rius, G.; Sort, J. Voltage-Induced ON Switching of Magnetism in Ordered Arrays of Non-Ferrimagnetic Nanoporous Iron Oxide Microdisks. *Adv. Mater. Interfaces* **2021**, *8* (1), No. 2001143.

(38) de h-Óra, M.; Nicolenco, A.; Monalisha, P.; Maity, T.; Zhu, B.; Lee, S.; Sun, Z.; Sort, J.; MacManus-Driscoll, J. Highly cyclable voltage control of magnetism in cobalt ferrite nanopillars for memory and neuromorphic applications. *APL Mater.* **2023**, *11* (5), No. 051105.

(39) Ma, Z.; Tan, Z.; Quintana, A.; Spasojevic, I.; López-Pintó, N.; Sánchez, F.; Fina, I.; Herrero-Martín, J.; Menéndez, E.; Sort, J. Ionic control of magnetism in all-solid-state CoOx/yttria-stabilized zirconia heterostructures. *Appl. Phys. Lett.* **2024**, *124*, No. 202404.

(40) Spasojevic, I.; Ma, A.; Barrera, A.; Celegato, F.; Palau, A.; Tiberto, P.; Buchanan, K. S.; Sort, J. Magneto-Ionic Vortices: Voltage-Reconfigurable Swirling-Spin Analog-Memory Nanomagnets. *arXiv:2403.13722.* 2024.

(41) Navau, C.; Sort, J. Exploiting random phenomena in magnetic materials for data security, logics, and neuromorphic computing: Challenges and prospects. *APL Mater.* **2021**, *9*, No. 070903.

(42) Lutterotti, L.; Scardi, P. Simultaneous structure and size−strain refinement by the Rietveld method. *J. Appl. Crystallogr.* **1990**, *23* (4), 246−252.

(43) Jain, A.; Ong, S. P.; Hautier, G.; Chen, W.; Richards, W. D.; Dacek, S.; Cholia, S.; Gunter, D.; Skinner, D.; Ceder, G.; Persson, K. A. Commentary: The Materials Project: A materials genome approach to accelerating materials innovation. *APL Mater.* **2013**, *1*, No. 011002.

(44) Ong, S. P.; Richards, W. D.; Jain, A.; Hautier, G.; Kocher, M.; Cholia, S.; Gunter, D.; Chevrier, V. L.; Persson, K. A.; Ceder, G. Python Materials Genomics (pymatgen): A robust, open-source python library for materials analysis. *Comput. Mater. Sci.* **2013**, *68*, 314−319.

(45) Hjorth Larsen, A.; Jørgen Mortensen, J.; Blomqvist, J.; Castelli, I. E.; Christensen, R.; Dułak, M.; Friis, J.; Groves, M. N.; Hammer, B.; Hargus, C.; Hermes, E. D.; Jennings, P. C.; Bjerre Jensen, P.; Kermode, J.; Kitchin, J. R.; Leonhard Kolsbjerg, E.; Kubal, J.; Kaasbjerg, K.; Lysgaard, S.; Bergmann Maronsson, J.; Maxson, T.; Olsen, T.; Pastewka, L.; Peterson, A.; Rostgaard, C.; Schiøtz, J.; Schütt, O.; Strange, M.; Thygesen, K. S.; Vegge, T.; Vilhelmsen, L.; Walter, M.; Zeng, Z.; Jacobsen, K. W. The atomic simulation environment-a Python library for working with atoms. *J. Phys.: Condens. Matter* **2017**, *29* (27), No. 273002.

(46) Giannozzi, P.; Andreussi, O.; Brumme, T.; Bunau, O.; Buongiorno Nardelli, M.; Calandra, M.; Car, R.; Cavazzoni, C.; Ceresoli, D.; Cococcioni, M.; Colonna, N.; Carnimeo, I.; Dal Corso, A.; de Gironcoli, S.; Delugas, P.; DiStasio, R. A.; Ferretti, A.; Floris, A.; Fratesi, G.; Fugallo, G.; Gebauer, R.; Gerstmann, U.; Giustino, F.; Gorni, T.; Jia, J.; Kawamura, M.; Ko, H. Y.; Kokalj, A.; Küçükbenli, E.; Lazzeri, M.; Marsili, M.; Marzari, N.; Mauri, F.; Nguyen, N. L.; Nguyen, H. V.; Otero-de-la-Roza, A.; Paulatto, L.; Poncé, S.; Rocca, D.; Sabatini, R.; Santra, B.; Schlipf, M.; Seitsonen, A. P.; Smogunov, A.; Timrov, I.; Thonhauser, T.; Umari, P.; Vast, N.; Wu, X.; Baroni, S. Advanced capabilities for materials modelling with Quantum ESPRESSO. *J. Phys.: Condens. Matter* **2017**, *29* (46), No. 465901.

(47) Perdew, J. P.; Burke, K.; Ernzerhof, M. Generalized Gradient Approximation Made Simple. *Phys. Rev. Lett.* **1997**, *78* (7), 1396.

(48) van Setten, J.; Giantomassi, M.; Bousquet, E.; Verstraete, M. J.; Hamann, D. R.; Gonze, X.; Rignanese, G.-M. The PseudoDojo: Training and grading a 85 element optimized norm-conserving pseudopotential table. *Comput. Phys. Commun.* **2018**, *226*, 39−54.

(49) Adamo, C.; Barone, V. Toward reliable density functional methods without adjustable parameters: The PBE0 model. *J. Chem. Phys.* **1999**, *110* (13), 6158−6170.

(50) Henkelman, G.; Uberuaga, B. P.; Jónsson, H. A Climbing Image Nudged Elastic Band Method for Finding Saddle Points and Minimum Energy Paths. *J. Chem. Phys.* **2000**, *113* (22), 9901−9904.

(51) Henkelman, G.; Jónsson, H. Improved tangent estimate in the nudged elastic band method for finding minimum energy paths and saddle points. *J. Chem. Phys.* **2000**, *113* (22), 9978−9985.

(52) Pellicer, E.; Pané, S.; Sivaraman, K. M.; Ergeneman, O.; Suriñach, S.; Baró, M. D.; Nelson, B. J.; Sort, J. Effects of the anion in glycine-containing electrolytes on the mechanical properties of electrodeposited Co−Ni films. *Mater. Chem. Phys.* **2011**, *130* (3), 1380−1386.

(53) Cabrera, N.; Mott, N. Theory of the Oxidation of Metals. *Rep. Prog. Phys.* **1949**, *12*, 163.

(54) Wagner, C. *Atom Movements*; ASM: Cleveland, 1951.

(55) Cañón, J.; Teplyakov, A. V. XPS characterization of cobalt impregnated SiO_2 and γ-Al_2O_3. *Surf. Interface Anal.* **2021**, *53* (5), 475−481.

(56) Fantauzzi, M.; Secci, F.; Sanna Angotzi, M.; Passiu, C.; Cannas, C.; Rossi, A. Nanostructured spinel cobalt ferrites: Fe and Co chemical state, cation distribution and size effects by X-ray photoelectron spectroscopy. *RSC Adv.* **2019**, *9*, 19171−19179.

(57) Sakamoto, K.; Hayashi, F.; Sato, K.; Hirano, M.; Ohtsu, N. XPS spectral analysis for a multiple oxide comprising NiO, TiO_2, and $NiTiO_3$. *Appl. Surf. Sci.* **2020**, *526*, No. 146729.

(58) Dubey, P.; Kaurav, N.; Devan, R. S.; Okram, G. S.; Kuo, Y. K. The effect of stoichiometry on the structural, thermal and electronic properties of thermally decomposed nickel oxide. *RSC Adv.* **2018**, *8*, 5882.

(59) de Rojas, J.; Quintana, A.; Lopeandía, A.; Salguero, J.; Costa-Krämer, J. L.; Abad, L.; Liedke, M. O.; Butterling, M.; Wagner, A.; Henderick, L.; Dendooven, J.; Detavernier, C.; Sort, J.; Menéndez, E. Boosting Room-Temperature Magneto-Ionics in a Non-Magnetic Oxide Semiconductor. *Adv. Funct. Mater.* **2020**, *30*, No. 2003704.

(60) Lebugle, A.; Axelsson, U.; Nyholm, R.; Martensson, N. Experimental L and M Core Level Binding Energies for the Metals ^{22}Ti to ^{30}Zn. *Phys. Scr.* **1981**, *23*, 825.

(61) Briggs, D. *Handbook of X-ray Photoelectron Spectroscopy*, Perkin-Elmer Corp. *Physical Electronics Division* **1981**.

(62) Powell, C. J.; Erickson, N. E.; Jach, T. Summary Abstract: Accurate determination of the energies of Auger electrons and photoelectrons from nickel, copper, and gold. *J. Vac. Sci. Technol.* **1982**, *20* (3), 625.

(63) Shalvoy, R. B.; Reucroft, P. J. Characterization of a sulfur-resistant methanation catalyst by XPS. *J. Vac. Sci. Technol.* **1979**, *16* (2), 567−569.

(64) Sarnecki, A.; Adamski, P.; Albrecht, A.; Komorowska, A.; Nadziejko, M.; Moszynski, D. XPS study of cobalt-ceria catalysts for ammonia synthesis − The reduction process. *Vacuum.* **2018**, *155*, 434−438.

(65) Salunkhe, P.; A V, M. A.; Kekuda, D. Investigation on tailoring physical properties of Nickel Oxide thin films grown by dc magnetron sputtering. *Mater. Res. Express* **2020**, *7* (1), No. 016427.

(66) Bagus, P. S.; Nelin, C. J.; Brundle, C. R.; Crist, B. V.; Ilton, E. S.; Lahiri, N.; Rosso, K. M. Main and Satellite Features in the Ni 2p XPS of NiO. *Inorg. Chem.* **2022**, *61* (45), 18077−180794.

(67) Deng, B.; Zhong, P.; Jun, K.; Riebesell, J.; Han, K.; Bartel, C. J.; Ceder, G. CHGNet as a pretrained universal neural network potential for charge-informed atomistic modelling. *Nat. Mach Intell* **2023**, *5*, 1031−1041.

(68) Quintana, A.; Menéndez, E.; Liedke, M. O.; Butterling, M.; Wagner, A.; Sireus, V.; Torruella, P.; Estradé, S.; Peiró, F.; Dendooven, J.; Detavernier, C.; Murray, P. D.; Gilbert, D. A.; Liu, K.; Pellicer, E.; Nogues, J.; Sort, J. Voltage-Controlled ON−OFF Ferromagnetism at Room Temperature in a Single Metal Oxide Film. *ACS Nano* **2018**, *12* (10), 10291−10300.

(69) Manukyan, K. V.; Avetisyan, A. G.; Shuck, C. E.; Chatilyan, H. A.; Rouvimov, S.; Kharatyan, S. L.; Mukasyan, A. S. Nickel Oxide Reduction by Hydrogen: Kinetics and Structural Transformations. *J. Phys. Chem. C* **2015**, *119* (28), 16131−16138.

■ NOTE ADDED AFTER ASAP PUBLICATION

This paper was published ASAP on January 20, 2025 with the surname "Rignanese" misspelled. The corrected version was reposted on January 31, 2025.